PAPER • OPEN ACCESS

Structure shape measurement method based on an optical fiber shape sensor

View the article online for updates and enhancements.

Structure shape measurement method based on an optical fiber shape sensor

Yuqi Tian[1] , **Hong Dang[2], Wenya Liu[1], Jiwen Cui[1,*], Yang Li[1] and Jiubin Tan[1]**

[1] Center of Ultra-precision Optoelectronic Instrument at Harbin Institute of Technology, Harbin 150080, People's Republic of China
[2] Electrical and Electronic Engineering at Southern University of Science and Technology, Shenzhen, 518055 Guangdong, People's Republic of China

E-mail: cuijiwen@hit.edu.cn

CrossMark

Abstract

In industry and architecture, real-time and complete measurement of structures has become a research frontier since it is directly related to the safety of life and property. Optical fibers have the potential to monitor constructions due to advantages such as small size, anti-electromagnetic interference, etc. However, existing research on optical fiber sensors pays attention to the sensing fiber itself and ignores the layout of the optical fibers. As a result, currently available fiber sensors are only suitable for monitoring one-dimensional rigid structures such as surgical robots and puncture needles. They may face challenges when measuring the freeform surfaces encountered in industrial and architectural scenarios. In this paper, a cross-orthogonal measurement method based on optical fiber shape sensors is proposed to meet the shape measurement requirements of freeform surfaces. The cross-orthogonal network allows global measurement and performs surface reconstructions more easily as compared to single-fiber arrays. It also divides the sensing fiber into several segments that are reconstructed separately (with different initial frames), avoiding the cumulative error at the end of the sensing fiber. Results of verification experiments using four-core fibers indicate that the presented method can improve measurement accuracy.

Keywords: shape on-line measurement, optical fiber shape sensor, surface structure shape measurement

(Some figures may appear in colour only in the online journal)

1. Introduction

Compared with metal materials, composite materials are increasingly being used in industrial and architectural fields due to their higher specific strength and rigidity [1, 2]. However, characteristics like small damping and low resonance frequency allow continuous shape change and low-frequency vibration after experiencing excitations such as height change and extreme temperature. At the same time, due to the nonlinearity and dispersion of material characteristics, it is exceedingly difficult to predict their strength or potential failure [3–5]. The above factors pose hidden risks to their systematic stability. Shape measurement technology is conducive to monitoring structural surfaces and effectively ensuring good system iteration [6, 7].

Optical fiber sensors are small in size, free from electromagnetic interference and easy to integrate, making them applicable for the shape measurement of minimally invasive medical surgical instruments, health monitoring of buildings

---

* Author to whom any correspondence should be addressed.

and industrial structures, and cable deformation monitoring [8, 9]. In these applications, the sensing fiber is routed along the object under test so that the object's shape can be derived from the pre-built mechanical model and the strain distribution along the sensing fiber. Following this idea, Ko *et al* regarded the sensing fiber as a cantilever beam to build a theoretical mechanical model and then realized the shape reconstruction through least squares fitting and the quadratic integral of the axial strain [10]. Pisoni *et al* calculated the weight of different deformations by introducing modal analysis [11]. The effectiveness of this approach was verified experimentally by Bogert and Haugse [12]. An accuracy improvement was observed because structural parameters were no longer required. Tessler and Spangler proposed an inverse finite element method [13] where the difference between the measured strain and the theoretically calculated strain gave weight to the least squares function. After that, Miller and Gherlone performed their own works to develop the inverse finite element method [14, 15]. However, these mechanical models only focus on a cantilever beam. For curves with higher degrees of freedom, the bending direction at each point may vary along the curve. In this case, the reconstruction of the curve requires that (1) the sensor can reflect the bending direction point by point and (2) the demodulation algorithm can update the extension direction of the curve from the measured torsion at each point.

Multi-core fiber provides a solution to the first problem. One can resolve the bending direction point by point from the difference in stress distributions of different cores. For the second problem, Moore proposed a Frenet frame based on the relation of differential geometry and then recovered the shape of the target by tracing the frames [16]. Later, Todd demonstrated that when the sensing fiber is stretched to an isolated position of zero curvature (isolated zeros), the orientation of the Frenet frame might change abruptly, thus affecting the accuracy of recovery results [17, 18]. Lim adjusted the Frenet frame at isolated zeros through a geometric derivation by equivalenting each micro-segment of the sensing fiber to a spiral [19, 20]. Cui *et al* proposed a rotation minimum frame (RMF) method to track the shape of the sensing fiber [21]. The key to the RMF algorithm is that the angular velocity of the frame around the curve remains zero in the tangential direction, thus avoiding the sudden change in frames at an isolated zeros surface frame. After that, the experiments done by Jackle further verified the RMF method, in which they correctly established the surface frames in sensing fibers with isolated zeros [22]. Lally *et al* measured the deflection of a 10 m-long flexible material plate using a sensing fiber with an S-shaped arrangement [23]. Moore *et al* measured the shape of flexible aerospace structures [24]. Although these approaches exhibited effectiveness in measuring complex deformations, their accuracy suffers from cumulative errors. In addition, the existing fiber sensors merely restore the shape of the sensing fiber itself, making them less intuitive in measuring the deformation of freeform surfaces.

To sum up, existing fiber shape sensors are mainly suitable for objects shaped in lines or curves (such as puncture needles and mechanical arms). For the shape reconstruction of freeform surfaces, the difficulties mainly include that (1) a single sensing fiber cannot measure the structure surface globally and (2) the accumulated error in the shape-demodulation process leads to poor accuracy at the end of the structure. This paper proposes a cross-orthogonal array of sensing fibers that allows global measurements and performs surface reconstructions more easily as compared to single-fiber arrays. It also divides the sensing fiber into several segments reconstructed separately (with different initial frames), avoiding the cumulative error at the end of the sensing fiber.

The first part of the paper is an introduction, which describes the development status of optical fiber shape sensors. The second section details the modified Frenet frame method at isolated zeros, which can smooth the frame along the sensing fiber. The third section demonstrates the shape measurement method based on differential geometry. The method is then further extended and applied to surface reconstruction in the fourth section. The fifth section is the experiment and analysis. The sixth section is the conclusion.

2. Establishment of the surface frame of a curve

According to the differential geometry principle, a smooth curve is well determined as its spatial shape parameters (including curvature and torsion) are known. For the four-core sensing fiber analyzed in this paper, we assume that (1) the integration of the fiber cores is solid without any gaps, (2) the mechanical properties of the fiber are consistent along the axis and (3) the mechanical properties of the fiber material are isotropic on cross section and the sensing fiber can be regarded as a Kirchhoff rod. The curvature and torsion along the fiber can be derived from the strain distribution.

Figure 1 depicts a micro-arc segment of a deformed fiber (with a bending radius equal to *R*). On the *A–A* cross section, we establish a Cartesian coordinate system at the fiber center. r_i and θ_i represent the distance from the origin and the deviation angle to the *x*-axis ($i = 1,2,3,4$ is the number of fiber cores); θ_b denotes the interior angle between the bending direction and the *x*-axis. According to [16], if fiber cores are spaced evenly around their center, then the curvature and torsion are:

$$
\begin{cases}
\kappa = \dfrac{2\,|\boldsymbol{\kappa}_{\text{app}}|}{M} \\
\theta_b = \arccos \dfrac{\boldsymbol{\kappa}_{\text{app},x}}{\boldsymbol{\kappa}_{\text{app}}} = \arcsin \dfrac{\boldsymbol{\kappa}_{\text{app},y}}{\boldsymbol{\kappa}_{\text{app}}} = \arctan \dfrac{\boldsymbol{\kappa}_{\text{app},y}}{\boldsymbol{\kappa}_{\text{app},x}}
\end{cases}
\tag{1}
$$

where,

$$
\boldsymbol{\kappa}_{\text{app}} = \sum_{i=1}^{M} \frac{\varepsilon_i}{r_i} \cos(\theta_i)\mathbf{i} + \sum_{i=1}^{M} \frac{\varepsilon_i}{r_i} \sin(\theta_i)\mathbf{j}.
\tag{2}
$$

M is the total number of cores. $\mathbf{i}$ and $\mathbf{j}$ represent the *x*-axis and *y*-axis directions, respectively. ε_i ($i = 1,2,3,4$) is strain along each core. The torsion of the curve is the derivative of the bending direction.
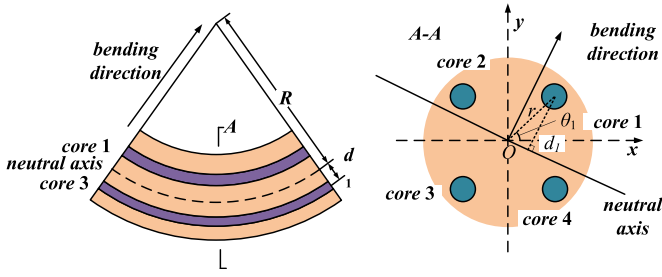
Figure 1. Measurement of curvature and torsion based on the geometric configuration of four-core fiber. (a) Schematic diagram of sensing optical fiber deformation. (b) Schematic diagram of the cross section of a sensing optical fiber.
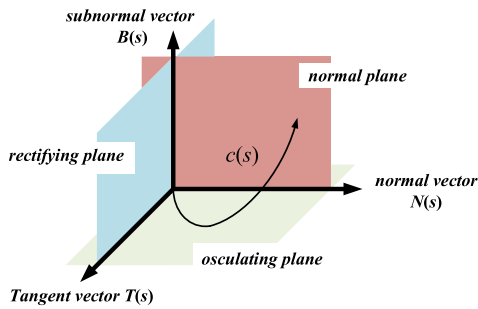
Figure 2. Schematic diagram of establishing a Frenet standard frame for a three-dimensional European space curve.

Taking equations (1)–(3) into the Frenet equation, we then have the Frenet frame:

$$
\begin{pmatrix} \boldsymbol{T}'(s) \\ \boldsymbol{N}'(s) \\ \boldsymbol{B}'(s) \end{pmatrix} = \begin{pmatrix} 0 & \kappa(s) & 0 \\ -\kappa(s) & 0 & \tau(s) \\ 0 & -\tau(s) & 0 \end{pmatrix} \begin{pmatrix} \boldsymbol{T}(s) \\ \boldsymbol{N}(s) \\ \boldsymbol{B}(s) \end{pmatrix}
$$

(3)

where $\boldsymbol{T}(s)$, $\boldsymbol{N}(s)$ and $\boldsymbol{B}(s)$ are the tangent, normal and bi-normal vectors, respectively (figure 2). In Frenet frames, $\boldsymbol{T}(s)$ represents the direction where the curve extends and $\boldsymbol{N}(s)$ and $\boldsymbol{B}(s)$ indicate the center of the bend. Therefore, the fiber shape can be recovered by tracking $\boldsymbol{T}(s)$ in most cases. At isolated zeros (e.g. point B in figure 3), $\boldsymbol{N}(s)$ and $\boldsymbol{B}(s)$ become singular, leading to uncertainty in the updating direction of $\boldsymbol{T}(s)$ (whether it is along the dotted curve or the solid curve) [17].

To solve this problem, we modify the normal vector in the Frenet frame. As shown in figure 3(b), we use the plus sign to reflect the fact that the angle between the bending direction of the micro-arc and the *x*-axis is less than $180°$; conversely, the minus sign indicates that the angle between the bending direction and the *x*-axis is over $180°$. Then, equation (3) is rewritten as

$$
\begin{pmatrix} \boldsymbol{T}'(s) \\ \boldsymbol{N}'_{\mathrm{m}}(s) \\ \boldsymbol{B}'_{\mathrm{m}}(s) \end{pmatrix} = \begin{pmatrix} 0 & \pm\kappa(s) & 0 \\ \mp\kappa(s) & 0 & \tau(s) \\ 0 & -\tau(s) & 0 \end{pmatrix} \begin{pmatrix} \boldsymbol{T}(s) \\ \boldsymbol{N}_{\mathrm{m}}(s) \\ \boldsymbol{B}_{\mathrm{m}}(s) \end{pmatrix}
$$

(4)

where $\boldsymbol{N}_{\mathrm{m}}(s)$ and $\boldsymbol{B}_{\mathrm{m}}(s)$ are the normal and bi-normal vectors after modification.
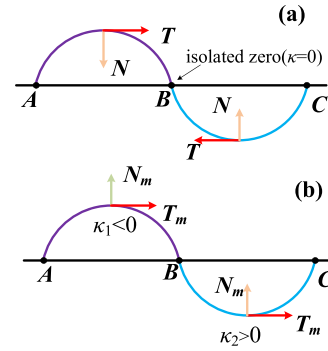

Figure 3. According to the positive and negative of the curvature, the direction of the normal vector will change. (a) When the curvature is positive, the normal vector points to the bending center. (b) When the curvature is negative, the normal vector points outward.
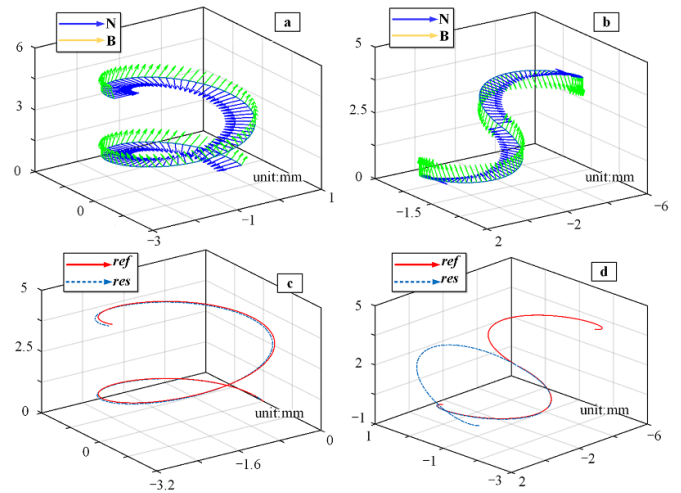
Figure 4. Simulation results using the Frenet algorithm. The curve in (a) is $c(t) = (1.5\cos(t), 1.5\sin(t), 0.5\,t)$, $t \in (0, 3\pi)$; the curve in (b) is divided into two sections, one of which is $c1(t) = (-1.5\cos(t)-3, 1.5\sin(t), 0.5\,t)$, $t \in (-1.5\pi, 0)$, the other is $c2(t) = (1.5\cos(t), 1.5\sin(t), 0.5\,t)$, $t \in (0, 1.5\pi)$, the intersection of two curves is an isolated singularity. (c) and (d) Tracking results of two cases.

Figure 3(b) demonstrates the updates of $\boldsymbol{N}_{\mathrm{m}}(s)$ and $\boldsymbol{T}_{\mathrm{m}}(s)$ near the isolated zero. It can be seen that the modified $\boldsymbol{N}_{\mathrm{m}}(s)$ is always on the same side along the extension of $\boldsymbol{T}(s)$. In other words, the above adjustment smooths jumps in the principal normal vectors at isolated zeros. As a consequence, $\boldsymbol{T}(s)$ at the next micro-arc can be well determined.

We further verify the validity of the smooth Frenet frame on continuous 3D curves. On the regular curves shown in figures 4(a) and (c), the curvatures of each point along the curve are non-zero. In these cases, the constructed and smooth Frenet frames are nearly identical. The reconstructed shapes of the sensing fiber are also consistent with the pre-sets. For comparison, when the curves under test contain isolated zeros, as shown in figures 4(b) and 5(a), the normal vectors recovered by the two algorithms are in opposite directions. Similarly, after tracing $\boldsymbol{T}(s)$, we find that the shape recovered based on the smooth Frenet frames is similar to the given curve, while the
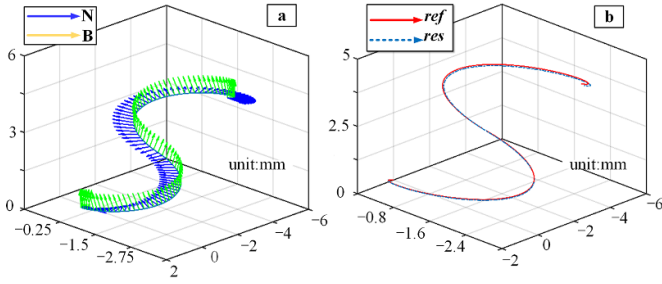
Figure 5. Frenet algorithm based on normal vector correction. (a) The curve is consistent with figure 4(b). (b) The result of curve reconstruction of the trace tangent vector.

Figure 6. Spatial surface establishment process.

Figure 7. Establishment process of a curved surface standard frame.

shape recovered based on the Frenet frames is quite different, as shown in figures 4(d) and 5(b). This reflects the fact that the adjustment algorithm proposed in this paper can enhance the universality of the Frenet frame.

3. Structural surface shape reconstruction

The structural frame can be determined based on an orthogonal sensing fiber. Next, we investigate how to restore the freeform surface from the shape of the sensing fiber. For this purpose, we establish a mapping between 2D and 3D Euclidean spaces (figure 6), establish the Cartesian coordinate systems (u, v) and (x, y, z) in two-dimensional and three-dimensional Euclidean space, respectively, and then the mapping relation r has the following general form:

$$\begin{cases} x = x(u,v), \\ y = y(u,v), \qquad (u,v) \in D \\ z = z(u,v), \end{cases} \quad (5)$$

where D is a connected open subset of 2D Euclidean space.

Here, we arrange the fiber orthogonally and specify the u and v parameters for longitude and latitude, respectively. In this case, the parametric relation can be further written in the form of $r = r(u(s),v(s))$. Then, the derivation of r at the microarc s_0 satisfies:
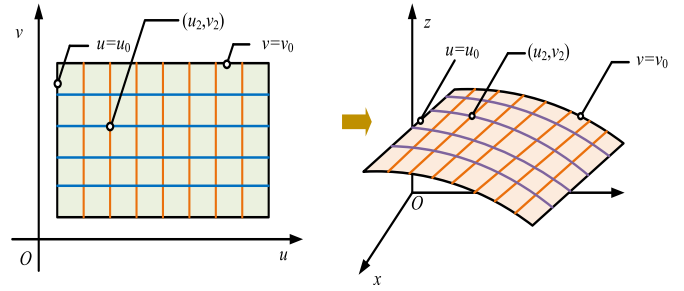
$$\frac{\mathrm{d}r}{\mathrm{d}s} = r_u \frac{\mathrm{d}u(s)}{\mathrm{d}t}\bigg|_{t=t_0} + r_v \frac{\mathrm{d}v(s)}{\mathrm{d}s}\bigg|_{s=s_0} \quad (6)$$

where $r_u = \partial r/\partial u$ and $r_v = \partial r/\partial v$ can be represented by the tangent vectors in the directions of latitude and longitude. Meanwhile, we can use the cross product of r_u and r_v to construct the unit vector perpendicular to them:
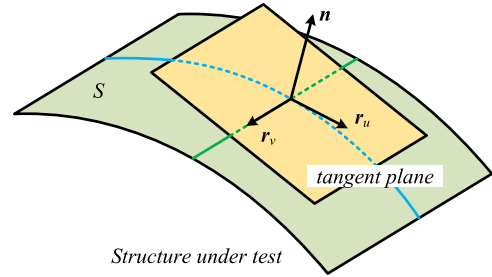
$$n(u,v) = \frac{r_u(u,v) \times r_v(u,v)}{|r_u(u,v) \times r_v(u,v)|}. \quad (7)$$

A set of frames used to characterize the surface is formed by r_u, r_v, and n, which is termed the surface frame, as shown in figure 7. We can trace the frames along the r_u and r_v directions to measure the whole structure shape.

In practical engineering applications, the sensing fiber is usually arranged on the surface of the structure in a serpentine

shape, but the measurement accuracy of the end of the structure is poor due to the accumulated error in the process of solving the Frenet frame. In this paper, a series of initial frames are introduced by setting a reference segment to solve the serpentine sensing optical fiber section by section, so as to reduce the number of operations and suppress the accumulated error. For segment v_0 in figure 6, a two-dimensional Cartesian coordinate system O_u is established on its cross section according to the rules that the x and y axes are parallel and perpendicular to the surface, respectively. According to equation (2):

$$\begin{aligned} \kappa_{\mathrm{app},x} &= \kappa \cdot \cos \theta_{\mathrm{B},v} \\ \kappa_{\mathrm{app},y} &= \kappa \cdot \sin \theta_{\mathrm{B},v} \end{aligned} \quad (8)$$

where $\theta_{\mathrm{B},v}$ represents the bending angle of the segment v_0 at this position; $\kappa_{\mathrm{app},x}$ and $\kappa_{\mathrm{app},y}$ are the components of the curvature vector on the x- and y-axes (in the positive direction). By orthogonalizing the units of $\kappa_{\mathrm{app},x}$ and $\kappa_{\mathrm{app},y}$ to obtain $\kappa_{Ov,x}$ and $\kappa_{Ov,y}$, a new frame composed of $\kappa_{Ov,x}$, $\kappa_{Ov,y}$, and T_{Ov} is obtained, and the subscript represents the O_v coordinate system. According to [21], this frame is the rotating minimum frame (RMF) of v_0. The Cartesian coordinate system O_u of the segment-$u_i(i = 1,2,3\ldots)$ intersected with the v_0 curve is established according to the same rules. Since the cross sections of the two sensing fibers are perpendicular to each other and $\kappa_{Ov,x}$ is perpendicular to O_u, $\kappa_{Ov,x}$ is same with the tangent vector T_{Ou} of the u_i curve at this position, as shown in figure 8. Due to O_u and O_v having the same establishment rules, $\kappa_{Ov,y}$ is the same as $\kappa_{Ou,y}$. Therefore, the following relationship exists: $\kappa_{Ou,x} = \kappa_{Ov,x} \times \kappa_{Ov,y} = T_{Ov}$. Through the above process, the RMF of the u_i curve is obtained by the frame of v_0 and the initial frame used to solve the Frenet frame group of u_i curve can be obtained by rotating around T_{Ov}:
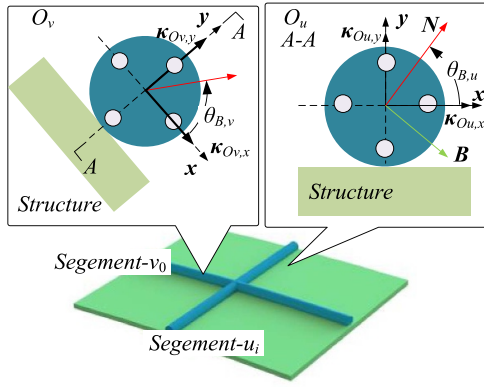
Figure 8. Establishment of the Frenet initial frame based on the reference curve.
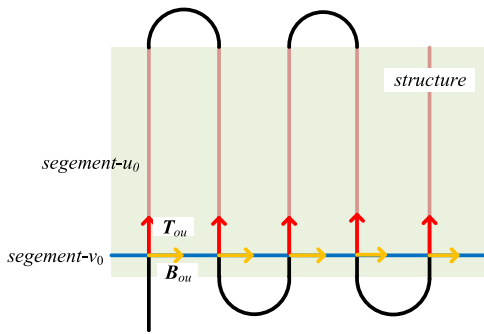
Figure 9. Schematic diagram of solving a serpentine sensing optical fiber.

$$\begin{bmatrix} \boldsymbol{T}_{Ou} \\ \boldsymbol{N}_{Ou} \\ \boldsymbol{B}_{Ou} \end{bmatrix} = \begin{bmatrix} 1 & 0 & 0 \\ 0 & \cos(\theta_{B,u}) & \sin(\theta_{B,u}) \\ 0 & -\sin(\theta_{B,u}) & \cos(\theta_{B,u}) \end{bmatrix} \begin{bmatrix} \boldsymbol{T}_{Ou} \\ \boldsymbol{\kappa}_{Ou,x} \\ \boldsymbol{\kappa}_{Ou,y} \end{bmatrix} \tag{9}$$

where $\theta_{B,u}$ represents the bending angle of the segment-u_i at this position.

Similarly, the initial frame of v_i can be obtained by using u_0, so we take u_0 and v_0 as reference segments. The advantage of this method is that the sensing fiber can be divided into several sections for separate solution through the reference segment, which effectively reduces the error of establishing the surface frames under certain spatial resolution and improves the measurement accuracy of the structure shape, as shown in figure 9.

Simulations are used to verify the effectiveness of the above structural shape reconstruction algorithm. Segments u and v are set as 19 and 12, respectively, the spatial resolution is 8 mm, and u_0 and v_0 are reference curves. We apply a force with an action distance of 5 mm to different positions at the end of the structure to make it bend or twist. Figures 10(a) and (b) show the schematic diagram of the arrangement of the optical fiber shape sensor. Taking (u_0, v_0) as the initial position, each component of the surface frame is $r_u = (1,0,0)$, $r_v = (0,1,0)$, $n = (0,0,1)$. The strain along each core is calculated by [25] and used for simulation. Figures 10(c) and

(d) depict the establishment results of surface frames, and figures 10(e) and (f) are the shape reconstruction results. For comparison, a single sensing fiber is set up to measure the shape of the structure in an S-shaped arrangement, as shown in figure 10(g). The simulation results are shown in figures 10(h) and (i).

The structure shape measurement method based on an optical fiber shape sensor is not limited to cantilever structures because the shape information of the structure is directly obtained. However, the information obtained by a single sensing fiber is limited in that it can only achieve local measurements of the structure. The structure shape measurement method based on the cross-orthogonal arrangement of double-sensing fibers can measure the shape of the structure globally. Since the Runge–Kutta algorithm is used to solve the Frenet differential equation, the measurement accuracy is only related to the accuracy and spatial resolution of strain measurement. Since the measurement accuracy and spatial resolution of strain cannot be improved infinitely, the proposed algorithm introduces a series of initial frames by setting reference segments to solve the S-shaped sensing fiber in segments. In this way, the cumulative error can be reduced by reducing the number of iterations needed to improve the final measurement accuracy. In addition, when the serpentine rotation section is ignored, the interval between fiber segments can be set smaller than that of the single sensing fiber measurement method so that the measurement points are more dense.

4. Experiment and analysis

Based on the previous analysis, the fiber shape sensor measures the strain in each direction of the sampling position through four fiber cores to obtain the curvature and torsion of the sensing fiber. Therefore, optical frequency domain reflection (OFDR) technology based on Rayleigh scattering was used to obtain the strain.

The optical path is shown in figure 11. The output of the tuned source laser (TLS; Yenista Tunics Reference) is split by coupler 1 into two beams, entering the main interferometer and auxiliary interferometer, respectively. The scanning range of the TSL is 20 nm and the spatial resolution of the OFDR system is 40 μm. To ensure stability in the strain measurement process, the spatial resolution of strain measurement is 8 mm (a measurement point contains 200 sampling points). The two signals are detected by a Thorlabs PDB450C-AC and collected by an Advantech PCI-1714UL acquisition card. The auxiliary interferometer signal zero crossing point is extracted for equal frequency sampling of the main interferometer signal to solve the reduction in strain measurement accuracy and spatial resolution caused by the frequency sweep nonlinearity of the tuned light source [25]. The interferometer is divided into a reference arm and a measuring arm by coupler 3. The sensing fiber to be measured is a four-core fiber (Chiral photonics, MCF-004_1), each core is separated by a fan-out
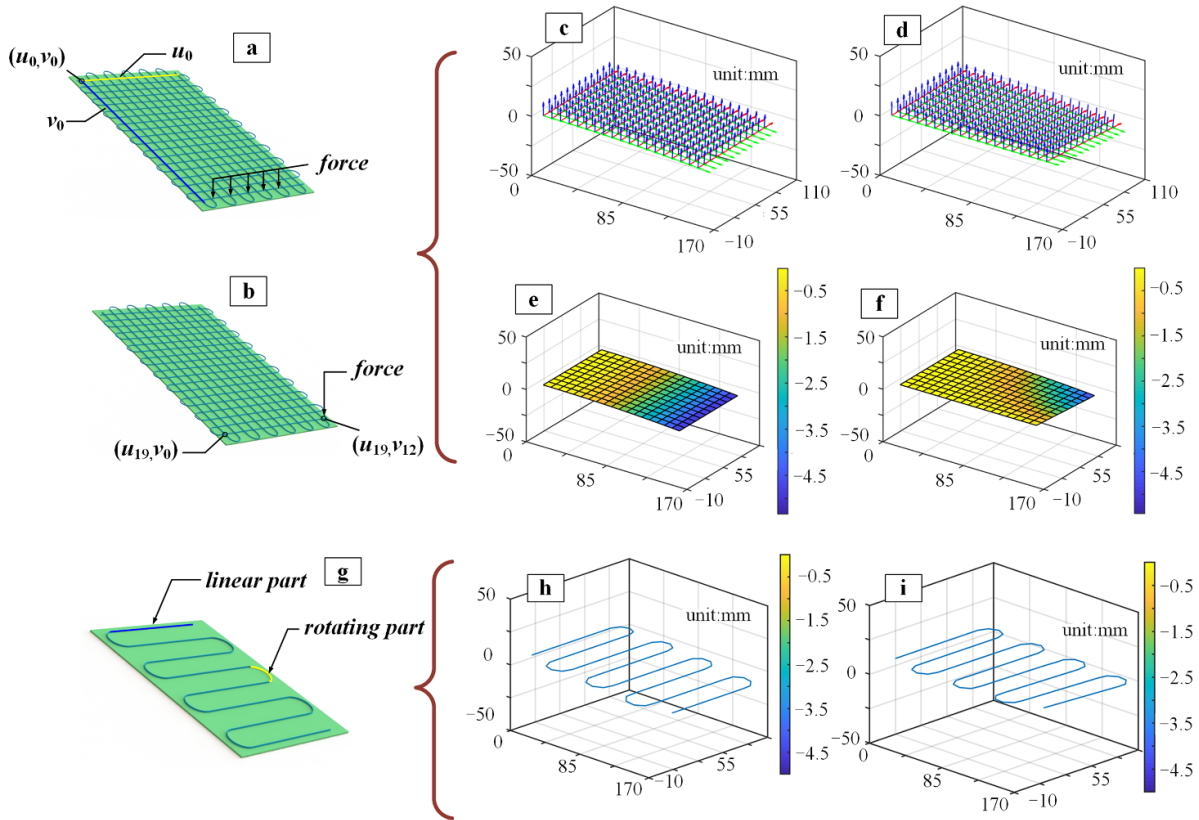
Figure 10. Simulation results of the mechanism shape measurement algorithm based on an optical fiber shape sensor. (a) and (b) The simulated structure under bending and torsional deformation respectively. (c) and (d) Establishment results of a curved surface local standard frame during bending and torsion, respectively. (e) and (f) The surface shape recovery results during bending and torsion, respectively. Figure 9(g) shows the structure with an optical shape four-core fiber arranged in an S-shape for comparison. Figures 9(e) and (f) show the reconstruction results.
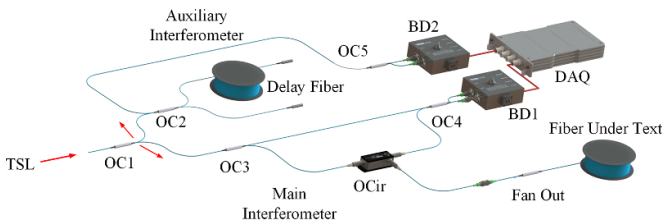
Figure 11. Optical frequency domain reflection strain demodulation based on Rayleigh scattering. OC: optical fiber coupler; OCir: optical circulator; BD: balance detector; DAQ: data acquisition; TSL: tuned source laser.
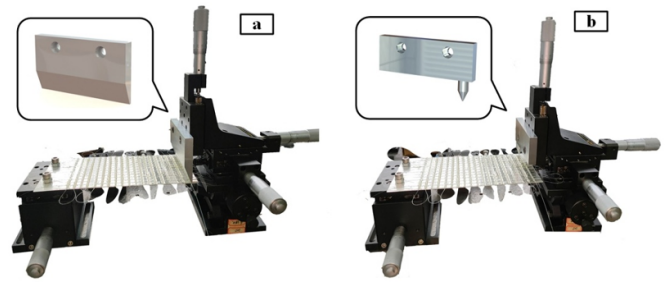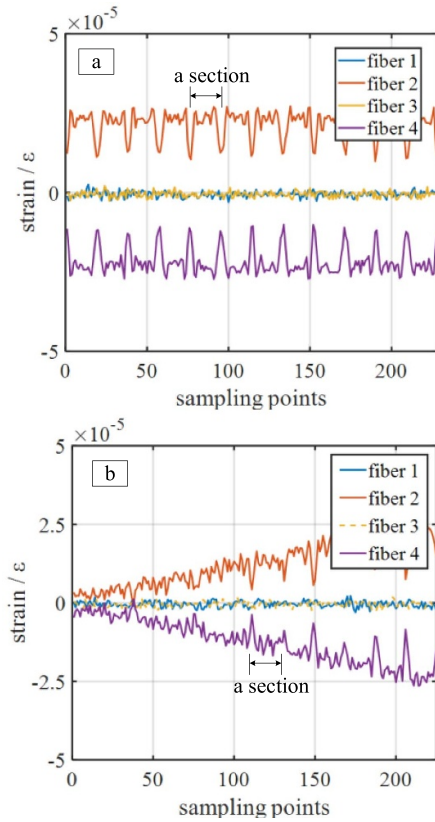

Figure 12. Experimental device. (a) Bending deformation. (b) Torsional deformation; the structure in the illustration is fixtures.

(Chiral Photonics MCFFO-s) and connected to the measuring arm by the circulator. Beat interference occurs when the reference light is in coupler 4 to obtain the Rayleigh spectrum of each core.

The two sensing fibers are packaged in an S-shape on a 160 mm × 100 mm × 0.5 mm aluminum plate with UV glue. Because the Young's modulus of UV glue is much smaller than that of sensing fiber, UV glue is softer than optical fiber, so the influence of UV glue is minimal. During the packaging process, it is ensured that the sensing fiber is not twisted and

taht the four cores are distributed on the *x*-axis and *y*-axis, as shown in figure 8. It should be noted that, as a reference, the sensing optical fiber at u_0 and v_0 should be strictly monitored to ensure there is no local torsion during the deployment process, otherwise its measurement accuracy will be affected. To accurately obtain the measurement error of the proposed method, an experimental device is built as shown in figure 12. The end of the plate acted through the displacement platform and the manufactured mechanical parts, with an action distance of 5 mm for comparison with the simulation results.

Figure 13. Strain along the four cores of fiber *v* under different deformation states. (a) Bending deformation. (b) Torsional deformation.

In this experiment, the sensing fiber *v* can more fully reflect the structural deformation, so the strain along the four cores of the sensing optical fiber *v* is shown in figure 13. Since the algorithm in this paper does not require the rotating section of an S-shaped sensing fiber, we do not show the strain in the rotating part due to the large curvature at these positions causing strain demodulation errors. It can be seen that since the bending direction is always consistent in each segment, cores 2 and 4 are mainly strained, which is consistent with the theoretical analysis in section 2. The strain along the four cores in each segment is similar under bending deformation due to the consistent curvature. While they gradually increase under torsional deformation because the curvature is getting bigger. In addition, the strain at the beginning and the end of each segment is the greatest, because the deformation is maximum here due to the load applied at these two positions.

Figure 14 shows the measurement results, in which (a), (b) and (c) represent when the structure is plane, bent or twisted. The unit of coordinate axis is millimeters. The spatial position error of the measurement point is defined as:

$$\delta = \sqrt{(x_{\text{sim}} - x_{\text{mea}})^2 + (y_{\text{sim}} - y_{\text{mea}})^2 + (z_{\text{sim}} - z_{\text{mea}})^2} \quad (10)$$

where x_{sim}, y_{sim} and z_{sim} represent the *x, y* and *z* coordinates of the simulation results, respectively; x_{mea}, y_{mea} and z_{mea} represent the *x, y* and *z* coordinates of the measurement results, respectively. According to the theoretical analysis, the

algorithm is to set the standard frame of (u_0, v_0) and then iterated backwards, so the position of the measurement point is based on the relative measurement value of (u_0, v_0). Therefore, (u_{18}, v_0), (u_0, v_{11}) and (u_{18}, v_{11}) are used to analyze the algorithm measurement error. By comparing with the simulation results, the measurement error is shown in table 1

Structural shape measurement results.

	(u_0, v_{11})	(u_{18}, v_0)	(u_{18}, v_{11})
Plane	0.50 mm	0.79 mm	0.85 mm
Bending	0.48 mm	0.90 mm	1.36 mm
Torsion	0.49 mm	0.80 mm	1.14 mm

When the sensing fibers are laid across the plate, there is a difference of one optical fiber diameter (125 μm) in the horizontal position. Due to the large bending radius of the tested structure during the deformation process, which is usually of the order of meters, the difference in horizontal position caused by the orthogonal arrangement of optical fibers can be ignored.

It should be noted that the reference segments u_0 and v_0 need to be strictly orthogonal to v_i and u_i, otherwise the error of the initial frame will lead to the calculation error of frames of v_i and u_i. However, the other positions do not need to be strictly orthogonal, because the normal vector of the surface is determined by the plane formed by r_u and r_v. The shape measurement method based on differential geometry is essentially realized by tracing the normal vector of the surface frame, so the accuracy of the frame establishment is a direct factor affecting the precision of shape measurement. It can be seen from Table 1 that the position errors of (u_0, v_{11}) under the three deformation conditions are basically the same; since segment u_0 is a reference curve and a straight line, the correctness of the Frenet frame on it is only affected by the strain measurement error, which will cause the accuracy of the curvature vector. For point (u_{18}, v_0), the spatial position error is the largest under bending conditions since the reference curve v_0 is deformed. In this case, the accuracy of the Frenet frame of the v_0 curve is not only affected by the strain measurement error, but also the iteration interval. Since the spatial resolution of the system based on OFDR is certain, the iteration interval of the Runge–Kutta algorithm leads to an error in the solution of the Frenet equation. For point (u_{18}, v_{11}), the accuracy of the surface frame at this position is affected by the error of the initial Frenet frame at points (u_0, v_{11}) and (u_{18}, v_0), resulting in a larger positional measurement error. In addition, for the plane case, the positional error of (u_{18}, v_{11}) is the smallest since the plane deformation reference lines v_0 and u_{18} are straight lines. For the torsion case, the error of the local standard frame at (u_{18}, v_{11}) is only introduced by solving curve u_{18} since v_0 and u_0 are straight (the accuracy of the initial Frenet frames at (u_{18}, v_0) and (u_0, v_{11}) are consistent with the plane case), resulting in a relatively small positional error. For the bending case, the initial Frenet frame at (u_{18}, v_0) has a greater error since v_0 is deformed under bending deformation, resulting in a maximum positional error
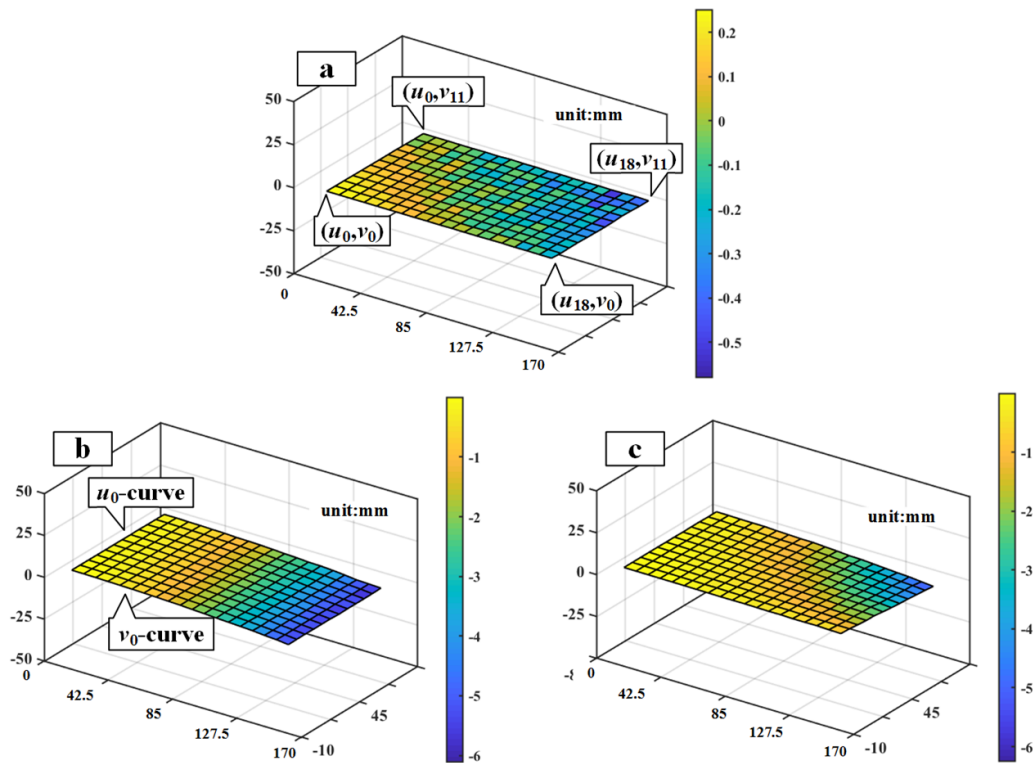
Figure 14. Structural shape measurement results: (a) measurement results of plane; (b) measurement results of bending; (c) measurement results of torsion.

of (u_{18}, v_{11}). In summary, the surface frame at any position is defined by the crossing of the tangent vector of segments u and v, iterated by the Frenet frame of the reference line as the initial standard frame. Consequently, the initial standard frame error directly affects the accuracy of the establishment of the surface frame at the subsequent position. An action distance of 5 mm is used for comparison with the simulation results. Since the deformation of the plate is known in the simulation, the measurement error can be accurately obtained by comparing the simulated displacement with the actual measured displacement.

5. Conclusion

Fiber optic shape sensors have been increasingly used in industrial applications. In this paper, a cross orthogonal arrangement method based on optical fiber shape sensors is proposed, which can achieve global shape measurement of a structure. In addition, because the reference fiber is set to introduce an initial frame to solve an optical fiber in segments, the solution length of the system can be reduced under the condition of a certain spatial resolution and the problem of large terminal accuracy error caused by accumulated errors is solved. Experiments and analysis show that the measurement results of the measurement method proposed in this paper have obvious advantages over the traditional methods and the maximum measurement error is only 1.36 mm.

Data availability statement

The data cannot be made publicly available upon publication because they are not available in a format that is sufficiently accessible or reusable by other researchers. The data that support the findings of this study are available upon reasonable request from the authors.

ORCID iD

Yuqi Tian ⓘ https://orcid.org/0000-0001-8951-1787

References

[1] Shanyi D 2007 Advanced composite materials and aerospace engineering *Acta Mater. Compos. Sin.* **24** 1–12
[2] Wu Z, Qu X, Gao D, Liu K and Feng J 2016 Research progress on structural health monitoring technology for aerospace composite structures *Aeronaut. Manuf. Technol.* **15** 92–102
[3] Housner G W, Bergman L A and Caughey T K Chassiakos A G, Claus R O, Masri S F and Yao J T 1997 Structural control: past, present, and future *J. Eng. Mech.* **123** 897–971

[4] Su Z, Ye L and Lu Y 2006 Guided Lamb waves for identification of damage in composite structures: a review *J. Sound Vib.* **295** 753–80

[5] Abdel-Jaber H and Glisic B 2015 Analysis of the status of pre-release cracks in prestressed concrete structures using long-gauge sensors *Smart Mater. Struct.* **24** 025–038

[6] Xia Y, Zhang P and Ni Y 2014 Deformation monitoring of a super-tall structure using real-time strain data *Eng. Struct.* **67** 29–38

[7] Lee J and Shinozuka M 2006 Real-time displacement measurement of a flexible bridge using digital image processing techniques *Exp. Mech.* **46** 105–14

[8] Culshaw B 2004 Optical fiber sensor technologies: opportunities and—perhaps—pitfalls *J. Light. Technol.* **22** 39

[9] Amanzadeh M, Aminossadati S M, Kizil M S and Rakić A D 2018 Recent developments in fibre optic shape sensing *Measurement* **128** 119–37

[10] Ko W L, Richards W L and Fleischer V T 2009 *Applications of KO Displacement Theory to the Deformed Shape Predictions of the Doubly-Tapered Ikhana Wing* (Edwards, CA: NASA Dryden Flight Research Center)

[11] Pisoni A C, Santolin C and Hauf D E Dubowsky S 1995 Displacements in a vibrating body by strain gauge measurements *Proc. SPIE* **8345** 83452Y

[12] Foss G C and Haugse E D 1995 Using modal test results to develop strain to displacement transformations *Proc. SPIE— Int. Soc. Opt. Eng.*

[13] Tessler A and Spangler J A 2003 Variational principle for reconstruction of elastic deformations in shear deformable plates and shells *National Aeronautics and Space Administration* (Hampton, VA: Langley Research Center)

[14] Miller E J, Manalo R and Tessler A 2016 Full-field reconstruction of structural deformations and loads from measured strain data on a wing using the inverse finite element method *NASA/TM-2016-219407* (NASA Langley Research Center)

[15] Esposito M and Gherlone M 2020 Composite wing box deformed-shape reconstruction based on measured strains: optimization and comparison of existing approaches *Aerosp. Sci. Technol.* **99** 105758

[16] Moore J P and Rogge M D 2012 Shape sensing using multi-core fiber optic cable and parametric curve solutions *Opt. Express* **20** 2967–73

[17] Todd M D, Stull C J and Dickerson M 2013 A local material basis solution approach to reconstructing the three-dimensional displacement of rod-like structures from strain measurements *J. Appl. Mech.* **80** 041028

[18] Todd M D, Stull C J and Dickerson M 2013 A locally exact strain-to-displacement approach for shape reconstruction of slender objects using fiber Bragg gratings *Proc. SPIE* **8693** 869302

[19] Lim S and Han S 2017 Helical extension method for solving the natural equation of a space curve *Surf. Topogr.: Metrol. Prop.* **5** 035002

[20] Lim S and Han S 2018 Shape estimation of a bent and twisted cylinder using strain from a sensor array in triple helices *Meas. Sci. Technol.* **29** 095003

[21] Cui J, Zhao S, Yang C and Tan J 2017 Parallel transport frame for fiber shape sensing *IEEE Photonics J.* **10** 1–12

[22] Jäckle S, Eixmann T, Schulz-Hildebrandt H, Hüttmann G and Pätz T 2017 Fiber optical shape sensing of flexible instruments for endovascular navigation *Int. J. Comput. Assist. Radiol. Surg.* **14** 2137–45

[23] Lally E M, Reaves M, Horrell E and Froggatt M 2012 Fiber optic shape sensing for monitoring of flexible structures *Proc. SPIE* **8345** 831–9

[24] Moore J P, Rogge M D and Jones T W 2012 Photogrammetric verification of fiber optic shape sensors on flexible aerospace structures *IEEE Avionics, Fiber-Optics and Photonics Technology Conf.* (*San Diego, CA, USA*, *12 November 2012*)

[25] Zhao S, Cui J, Yang C, Ding Z and Tan J 2017 Simultaneous measurement of shape and temperature in the substrate-attaching-fibers sensing system *IEEE Photon. J.* **9** 1–9

[26] Tian Y, Cui J, z X and Tan J 2022 Generalized cross-correlation strain demodulation method based on local similar spectral scanning *Sensors* **22** 5378